Flutter Prediction Based on Fully Coupled Fluid-Structural Interactions

Xiangying Chen*, Ge-Cheng Zha†, and Zongjun Hu‡
Dept. of Mechanical and Aerospace Engineering
University of Miami
Coral Gables, Florida 33124

Ming-Ta Yang§
Discipline Engineering - Structures
Pratt & Whitney
400 Main Street, M/S 163-07
East Hartford, CT 06108

Abstract

A fully coupled numerical methodology is developed for calculating the flow-structure interaction problems and is used to predict transonic airfoil flutter. The Roe scheme is extended to moving grid and used with the finite-volume method. The unsteady solutions march in time by using a dual-time stepping implicit unfactored Gauss-Seidel iteration. The unsteady Navier-Stokes equations and the linear structural equations are fully coupled implicitly via successive iteration with pseudo time stepping. The moving mesh and mesh deformation strategy is based on two mesh zones, a fine mesh zone surrounding the solid body without mesh deformation and a coarse mesh zone surrounding the fine mesh zone and deforms with the solid object. This mesh deformation strategy can maintain the orthogonality of the mesh near the wall and save CPU time for re-meshing. The study cases presented include a vortex-induced oscillating cylinder, a forced pitching airfoil, and an elastically mounted transonic airfoil. For the elastic transonic airfoil, the flutter boundary is calculated. Other phenomena captured include the limit cycle oscillation (LCO) and the steady state flow conditions, under which the aerodynamic forces and moments are balanced by the structure. The computational results agree well with the experiments and the computed results of other researchers. The methodology is demonstrated to be accurate, robust and efficient.

1 Introduction

Flow induced structural vibration is one of the most critical technical problems affecting the reliability, cost and safety of aircraft. Due to the very complicated non-linear flow-structure interaction and multidisciplinary (fluid and structure) requirements, there is a lack of high fidelity computational tools to study the basic physics and to predict the structural failure. The problems exist in both the airframe and aircraft engine systems. The situation is worse for the aircraft engine turbomachinery than airframe because the latter has numerous blades and the flow induced structural vibration is more complicated. This paper is aimed at developing a high fidelity predicting methodology for flow induced vibration in aircraft engine turbomachinery.

* Post Doctoral Associate, E-mail: xychen@apollo.eng.miami.edu
† Associate Professor, E-mail: zha@apollo.eng.miami.edu
‡ PhD Student, E-mail: zjhu@apollo.eng.miami.edu
§ Principal Engineer, E-mail: yangm@pweh.com

There are generally two types of methods to calculate the fluid-structure interaction problems: the fluid and structure governing equations are loosely coupled or fully coupled. The loosely coupled model means that the structural response lags behind the flow field solution. Within a time step for the loosely coupled method, the structure solver calculates the response after the flow solver is converged. This kind of methods may be limited to first-order temporal accuracy only regardless of the temporal accuracy of the individual solvers[1]. The fully coupled model is that the flow field and structure always respond simultaneously by exchanging the aerodynamic forcing and structural displacement within each inner iteration of a time step. Obviously, only the fully coupled model is rigorous in physical sense. Due to the complicated non-linear fluid-structure interaction phenomenon in turbomachines such as transonic stall flutter, oscillating shock waves and flow separation, etc., the fully coupled model between the fluid and structure system is necessary and is selected for this research to achieve high accuracy.

Recently, efforts have been started to develop the predicting capability for flow induced vibration. Bendiksen et al.[2] pioneered the research by using an explicit CFD code coupled with a structural integrator based on the convolution integral to obtain the flutter boundary for a NACA 64A010 airfoil. The loosely coupled model between the fluid and structural solvers include the work of Guruswamy[3], Lee-Rausch et al.[4], Smith[5], Vermeersch et al.[6], Darracq, et. al [7], Prananta, et. al[8], Bohbot et al.[9], and Blom et al.[10]. Alonso and Jameson developed a model which is close to the fully coupled method with the structural displacement updated every several fluid solver iterations[11]. The implicit Runge-Kutta method with multigrid acceleration is employed for the flow solver in Alonso's work[11][12]. In 1997-98, Morton and Melville et al. developed a implicit fully coupled fluid structural interaction model, which used the Beam-Warming implicit scheme for the flow solver coupled with modal structural solver [13][14][1]. In 2000, Liu et al. developed a fully coupled method using Jameson's explicit scheme with multigrid method and a finite element structural model [15].

The present study is to develop a fully coupled fluid-structure interaction model using different numerical techniques to achieve high accuracy and efficiency.

The implicit unfactored Gauss-Seidel iteration is used, which does not have factorization error and can allow very large (pseudo) time step to have fast convergence rate.

Both the model of Morton and Melville et al.[13][14] [1] and Liu et al. [15] employ the central differencing with an artificial dissipation model for the inviscid fluxes terms. The aerodynamic damping for a flow induced vibration is sensitive to different artificial dissipation which many vary case by case. Hence the central differencing with adjusted artificial dissipation may increase the uncertainty of the results. The present paper extends the high accuracy upwind Riemann solver of Roe to moving grid system in order to capture the high resolution unsteady shock waves and boundary layers. The Roe scheme has inherent low numerical dissipation and no adjustment of the numerical dissipation is needed for different problems.

The mesh deformation in the present method is different from the previous methods, which are based on the spring network and the mesh deformation occurs directly on the solid body surface. In the present method, the mesh is divided into tow zones. One is the fine mesh zone surrounding the solid body and moves with the solid object rigidly without deformation. The other is the coarse mesh zone surrounding the fine mesh zone and deforms following the motion of the solid object and its adjacent fine mesh zone. The advantages of this mesh deformation is that the orthogonality of the mesh near the wall is maintained and the fine mesh near the solid wall does not need to be regenerated by solving a Poisson equation. For a fluid-structure interaction problem, the mesh needs to be changed for each iteration when the structure is deformed. Therefore, avoiding regenerating the mesh near solid wall saves a significant amount of CPU time.

In this paper, the newly developed methodology is proved to be robust, accurate and efficient by the computed cases of a vortex-induced oscillating cylinder, a transonic pitching airfoil and an elastically mounted NACA 64A010 airfoil.

2 CFD Aerodynamic Model

2.1 Flow Governing Equations

The governing equations for the flow field computation are the Reynolds-Averaged Navier-Stokes equations (RANS) with Favre mass average which can be transformed to the generalized coordinates and expressed as:

$$\frac{\partial \mathbf{Q}'}{\partial t} + \frac{\partial \mathbf{E}'}{\partial \xi} + \frac{\partial \mathbf{F}'}{\partial \eta} + \frac{\partial \mathbf{G}'}{\partial \zeta} = \frac{1}{Re}\left(\frac{\partial \mathbf{E}'_{\mathbf{v}}}{\partial \xi} + \frac{\partial \mathbf{F}'_{\mathbf{v}}}{\partial \eta} + \frac{\partial \mathbf{G}'_{\mathbf{v}}}{\partial \zeta}\right) \tag{1}$$

where Re is the Reynolds number and

To save space, the detailed terms will not be given here and can be found in the literature or textbook[16] for the Navier-Stokes equations for moving grid. The turbulent shear stresses and heat flux appeared in above equations are calculated by Baldwin-Lomax model[17]. The viscosity is composed of $\mu + \mu_t$, where μ is the molecular viscosity and μ_t is the turbulent viscosity determined by Baldwin Lomax model. For a laminar flow, the μ_t is set to be zero.

2.2 Time Marching Scheme

The time dependent governing equation (1) is solved using the control volume method with the concept of dual time stepping suggested by Jameson[18]. A pseudo temporal term $\frac{\partial \mathbf{Q}}{\partial \tau}$ is added to the governing equation (1). This term vanishes at the end of each physical time step, and has no influence on the accuracy of the solution. However, instead of using the explicit scheme as in [18], an implicit pseudo time marching scheme using Gauss-Seidel iteration is employed to achieve high CPU efficiency. For unsteady time accurate computations, the temporal term is discretized implicitly using a three point, backward differencing as the following

$$\frac{\partial \mathbf{Q}}{\partial t} = \frac{3Q^{n+1} - 4Q^n + Q^{n-1}}{2\Delta t} \tag{2}$$

Where n is the time level index. The pseudo temporal term is discretized with first order Euler scheme. Let m stand for the iteration index within a physical time step, the semi-discretized governing equation (1) can be expressed as

$$[(\frac{1}{\Delta\tau} + \frac{1.5}{\Delta t})I - (\frac{\partial R}{\partial Q})^{n+1,m}]\delta Q^{n+1,m+1} = R^{n+1,m} - \frac{3Q^{n+1,m} - 4Q^n + Q^{n-1}}{2\Delta t} \tag{3}$$

where the $\Delta\tau$ is the pseudo time step, R is the net flux going through the control volume,

$$R = -\frac{1}{V}\int_s [(F - F_v)\mathbf{i} + (G - G_v)\mathbf{j} + (H - H_v)\mathbf{k}]\cdot d\mathbf{s} \tag{4}$$

where V is the volume of the control volume, $\mathbf{s}$ is the control volume surface area vector. Equation (3) is solved using the unfactored Gauss-Seidel iteration. The method is unconditionally stable and can reach very large pseudo time step since no factorization error is introduced.

The Roe scheme[19] is selected and implemented in the code to evaluate the inviscid fluxes with the 3rd order MUSCL type differencing[20].

It can be proved that the eigenvector matrix of the Roe scheme in the moving grid is exactly the same as the one without moving grid. The only difference between the moving grid and the stationary grid system is that, for the moving grid system, the contravariant velocity in the eigenvalues contains the grid velocity. It

is hence straightforward to extend the code from a stationary grid system to the moving grid system using Roe scheme.

The grid velocity is evaluated at the center of each cell and is determined by the averaged value that counts all the movement at eight vertexes if hexahedral control volumes are used. The grid velocity is reconstructed with 3rd MUSCL differencing.

It was pointed out by Thomas et al.[21] that due to the mixed temporal and spatial derivatives after discretization, an additional term appears, which theoretically equals to zero but numerically still remains. Consequently numerical error could be introduced in the discretized form of the equations of the flow motion if this term is neglected. In order to reduce or avoid this error, the geometric conservation law is enforced by solving an additional equation[21]. As has been observed, the overall performance of this numerical supplement is beneficial with very little CPU time cost.

2.3 Boundary Conditions

The flow field is solved subject to appropriate boundary conditions described as bellow:

(1) Upstream boundary conditions: The outer boundary is divided into upstream and downstream boundaries according to whether the direction of its segment is toward or backward to the incoming flow direction. On upstream boundary, it is assumed that the streamwise velocity u is uniform, and transverse velocity $v = 0$. Other primitive variables are specified according to the freestream condition except the pressure which is extrapolated from interior.

(2) Downstream boundary conditions: All the flow quantities are extrapolated from interior except the pressure which is set to be its freestream value.

(3) Solid wall boundary conditions: At moving boundary surface, the no-slip condition is enforced by extrapolating the velocity between the phantom and interior cells,

$$u_0 = 2\dot{x}_b - u_1, \qquad v_0 = 2\dot{y}_b - v_1 \tag{5}$$

where u_0 and v_0 denote the velocity at phantom cell, u_1 and v_1 denote the velocity at the $1st$ interior cell close to the boundary, and u_b and v_b are the velocity on the moving boundary.

The other two conditions to be imposed on the solid wall are the adiabatic wall condition and the inviscid normal momentum equation[13] as follows,

$$\frac{\partial T}{\partial \eta} = 0, \qquad \frac{\partial p}{\partial \eta} = -\left(\frac{\rho}{\eta_x^2 + \eta_y^2}\right)(\eta_x \ddot{x}_b + \eta_y \ddot{y}_b) \tag{6}$$

2.4 Moving/Deforming Grid Systems

For both the cylinder and airfoil cases, the computational domains are divided into two regions, namely the fine mesh zone and the coarse mesh zone. The fine mesh zone surrounds the solid body of the object and the coarse mesh zone surrounds the fine mesh zone. In order to capture the details of the boundary layer flow, a large number of grid points are distributed around the object surface in the fine mesh zone. The outer flow field has smaller gradient, it hence can be computed using a coarser mesh to reduce the CPU time.

When the structure deforms due to the fluid forcing, the fine mesh zone moves rigidly with the object with no deformation, and the coarse mesh zone covers the rest of computational domain by distorting its grids. The far field boundary is fixed with no motion. That is, the outer zone mesh deforms with the motion of the inner zone mesh as a spring network system.

There are two advantages for handling the moving mesh systems using the present strategy : 1) the refined mesh around the object body is the same throughout the simulation and the same accuracy can be achieved

around the moving object regardless of the position of the object. The mesh orthogonality is maintained; 2) the CPU time can be saved by avoiding re-meshing the fine mesh region, where the Poisson equation needs to be solved for interior node points of the mesh for each iteration. For fluid-structure interaction problem, the mesh needs to be changed for each iteration when the structure is deformed. Therefore, avoiding regenerating the mesh near solid wall saves a significant amount of CPU time.

3 Structural Models

3.1 Elastic Cylinder

For the computations of the vortex-induced oscillating cylinder, which is elastically supported as shown in Figure 1 so that it oscillates only in the direction aligned with or normal to the incoming flow, the structural dynamic equations which govern the motion of the cylinder are:

$$m\ddot{x} + C_x\dot{x} + K_x x = D \tag{7}$$

$$m\ddot{y} + C_y\dot{y} + K_y y = L \tag{8}$$

These equations are solved implicitly together with the equations of flow motion, Equation (3), in a fully coupled manner. In Equation (7), $\ddot{x}$, $\dot{x}$, and x represent the dimensionless horizontal acceleration, velocity and displacement of the moving object respectively. Similarly, $\ddot{y}$, $\dot{y}$, and y in Equation (8) represent their corresponding ones in vertical direction. m, L, and D are the mass, lift, and drag per unit span respectively, C_x and C_y are the damping coefficients in horizontal and vertical directions, K_x and K_y are the spring constants in horizontal and vertical directions. In present study, this 'self-excited oscillators' is designed to have the same response in both direction, i.e. $C_x = C_y$ and $K_x = K_y$.

If the normalization procedure is applied to Equations (7) and (8) by using the same reference scales of those used for the equations of flow motion, the following nondimensional equations are obtained

$$\ddot{x} + 2\zeta\left(\frac{2}{\bar{u}}\right)\dot{x} + \left(\frac{2}{\bar{u}}\right)^2 x = \frac{2}{\mu_s\pi}C_d \tag{9}$$

$$\ddot{y} + 2\zeta\left(\frac{2}{\bar{u}}\right)\dot{y} + \left(\frac{2}{\bar{u}}\right)^2 y = \frac{2}{\mu_s\pi}C_l \tag{10}$$

where ζ is the nondimensional structural damping coefficient calculated by $\zeta = \frac{C_{x,y}}{2\sqrt{mK_{x,y}}}$, $\bar{u}$ is the reduced velocity defined by $\bar{u} = \frac{U_\infty}{b\omega}$, b is radius of the cylinder, $\omega = \sqrt{K_{x,y}/m}$, the mass ratio, $\mu_s = \frac{m}{\pi\rho_\infty b^2}$, C_d and C_l are the drag and lift force coefficients respectively. Then the equations are transformed to a matrix form and expressed by

$$[\mathbf{M}]\frac{\partial\{\mathbf{S}\}}{\partial t} + [\mathbf{K}]\{\mathbf{S}\} = \mathbf{q} \tag{11}$$

where

$$\mathbf{S} = \begin{pmatrix} x \\ \dot{x} \\ y \\ \dot{y} \end{pmatrix},\ \mathbf{M} = [I],\ \mathbf{K} = \begin{pmatrix} 0 & -1 & 0 & 0 \\ \left(\frac{2}{\bar{u}}\right)^2 & 2\zeta\left(\frac{2}{\bar{u}}\right) & 0 & 0 \\ 0 & 0 & 0 & -1 \\ 0 & 0 & \left(\frac{2}{\bar{u}}\right)^2 & 2\zeta\left(\frac{2}{\bar{u}}\right) \end{pmatrix},\ \mathbf{q} = \begin{pmatrix} 0 \\ \frac{2}{\mu_s\pi}C_d \\ 0 \\ \frac{2}{\mu_s\pi}C_l \end{pmatrix}.$$

To couple the structural equations with the equations of flow motion and solve them implicitly in each physical time step, above equations are discretized and integrated in a manner consistent with Equation (3) to yield

$$\left(\frac{1}{\Delta\tau}\mathbf{I}+\frac{1.5}{\Delta t}\mathbf{M}+\mathbf{K}\right)\delta S^{n+1,m+1}=-\mathbf{M}\frac{3\mathbf{S}^{n+1,m}-4\mathbf{S}^{n}+\mathbf{S}^{n-1}}{2\Delta t}-\mathbf{K}\mathbf{S}^{n+1,m}+\mathbf{q}^{n+1,m+1} \tag{12}$$

where n is the physical time level index while m stands for the pseudo time index. The detailed coupling procedure between the fluid and structural systems is given in section 4.

3.2 Elastic Airfoil

Unlike the structural model of the vortex-induced oscillating cylinder, the system of the elastically mounted airfoil is assumed to be undamped. The airfoil is allowed to move in pitch about a given elastic axis and plunge vertically. The pitch axis is defined by a distance a, which is the multiple of the semi-chord length with the origin point located at the mid-chord position. If a is positive, it means the axis is located downstream of the mid-chord, negative means being located upstream of the mid-chord point.

A sketch of the elastically mounted airfoil is depicted in Figure 2. The motion of such an elastic system can be described by using the following equations

$$m\ddot{h}+S_\alpha\ddot{\alpha}+K_h h=-L \tag{13}$$

$$S_\alpha\ddot{h}+I_\alpha\ddot{\alpha}+K_\alpha\alpha=M \tag{14}$$

where h and α are the plunging and pitching displacements respectively, m is the mass per unit span, S_α is the static moment around the elastic axis, I_α is the rotational moment of inertia, K_h and K_α are plunging and pitching spring constants respectively, L is the lift force and M is the moment around the elastic axis. The equations of the structure motion (13) and (14) are normalized by using semi-chord b as the length dimension, the uncoupled natural frequency in pitch ω_α as the time scale, and are expressed as

$$\ddot{h}+x_\alpha\ddot{\alpha}+\left(\frac{\omega_h}{\omega_\alpha}\right)^2 h=-\frac{U^{*2}}{\mu\pi}C_l \tag{15}$$

$$x_\alpha\ddot{h}+r_\alpha^2\ddot{\alpha}+r_\alpha^2\alpha=\frac{U^{*2}}{\mu\pi}C_m \tag{16}$$

where x_α is the static unbalance, ω_h is the uncoupled natural frequency in plunge, r_α^2 is the squared radius of gyration, U^* is the reduced velocity defined as $\frac{U_\infty}{\omega_\alpha b}$, C_l and C_m are the lift and moment coefficient respectively. Since the time scale used in Equations (15) and (16) is different from the one used in the governing equations of flow, the structural dimensionless time t_s^* needs to be re-scaled and keep its consistency with the entire system during the computation, i.e., $t_s^*=\frac{\omega_\alpha L}{U_\infty}t_f^*$, where t_f^* is the dimensionless time for flow and the L is the length scale. Finally the equations are cast into the form of Equations (11) and (12), and the corresponding matrices are

$$\mathbf{S}=\begin{pmatrix} h \\ \dot{h} \\ \alpha \\ \dot{\alpha} \end{pmatrix},\ \mathbf{M}=\begin{pmatrix} 1 & 0 & 0 & 0 \\ 0 & 1 & 0 & x_\alpha \\ 0 & 0 & 1 & 0 \\ 0 & x_\alpha & 0 & r_\alpha^2 \end{pmatrix},\ \mathbf{K}=\begin{pmatrix} 0 & -1 & 0 & 0 \\ \left(\frac{\omega_h}{\omega_\alpha}\right)^2 & 0 & 0 & 0 \\ 0 & 0 & 0 & -1 \\ 0 & 0 & r_\alpha^2 & 0 \end{pmatrix},\ \mathbf{q}=\begin{pmatrix} 0 \\ -\frac{U^{*2}}{\mu\pi}C_l \\ 0 \\ \frac{U^{*2}}{\mu\pi}C_m \end{pmatrix}.$$

4 Flow-Structure Coupling

Within a physical time step, the structural motion and the flow field are unknown and are solved iteratively between the fluid and structural systems in a fully couple manner. The following is the procedure:

(1) The variables at new time level $n+1$ of the flow and structural equations are initially set to the values of time level n.

(2) Calculate the aerodynamic forces including lift, drag, and torque exerting on the solid body of the object.

(3) Determine the position of the moving object subject to the aerodynamic forces by solving the structural equations.

(4) Re-generate the mesh and calculate the grid velocity at each node point according to the updated structural position.

(5) Calculate the flow field by solving the equations of flow motion for the updated mesh and structural position.

(6) Check the maximum residuals for both solutions of the flow and the structural equations. If the maximum residuals are greater than the prescribed convergence criteria, go back to step (2) and proceed to the next pseudo time level $m+1$, otherwise the flow field and the movement of the moving object are determined and go back to step (1) to start the next new physical time step $n+1$. The procedure can be also seen in the flow chart given in Figure 3.

5 Results and Discussion

The numerical results for the calculated 2-D problems are presented and discussed in this section. The vortex-induced oscillating cylinder is presented first. Then a transonic forced pitching airfoil and flow-induced vibration of the same airfoil are presented.

5.1 Vortex-Induced Oscillating Cylinder

The stationary cylinder is calculated first to verify the accuracy of the code, to determine the appropriate mesh dimension, and to provide the initial flow field for the oscillating cylinder.

5.1.1 Stationary Cylinder

The fine mesh zone mentioned in the previous section for the computation of vortex-induced oscillating cylinder is shown in Figure 4. The Reynolds number based on the free-stream condition and cylinder diameter is $Re = 500$. The free-stream Mach number is $M_\infty = 0.2$. The far field boundary is located 20 diameters away from the center of the cylinder. To resolve the boundary layer effect, very fine grids are clustered to the cylinder surface with first grid spacing in radial direction $\simeq 0.0005$ diameter.

Three different mesh dimensions are used to conduct the mesh refinement study for the stationary cylinder. Table 1 shows that the mesh with the dimensions of 120×80 in circumferential and radial directions can resolved the flow field with a satisfactory accuracy and is converged based on the mesh refinement study. This mesh is then used as the baseline mesh for all the computations involving flow past a cylinder.

After a short transition period, the coherent vortex shedding is formed and convected downstream of the cylinder without imposing any perturbation. Consequently, the lift and torque coefficients oscillate at certain frequency in terms of the Strouhal number defined as $St = \frac{fD}{U_\infty}$ where D is cylinder diameter and f is the frequency. The predicted drag coefficient oscillates with twice of the lift frequency. The computed Strouhal number, drag, lift and torque coefficients are given in Table 1. As can be seen in Table 1, the computed lift Strouhal number agrees accurately with the experimental results of Roshko[22] and Goldstein[23]. The corresponding numerical results with the mesh dimension of 384×96 by Alonso et al.[12] using central differencing with artificial dissipation are also listed in the table for comparison. The frequency in term of St_{C_l} predicted by the present method is significantly more accurate than the results of Alonso et al.[12], whose grid size is 3.84 times larger. The computed time histories of the drag and lift coefficients is plotted in Figure 5, which shows that perfect periodicity in time is achieved.

Table 1: Results of Mesh Refinement Study and comparison with the experiments

Mesh Dimension	St_{C_d}	St_{C_l}	St_{C_m}	C_l	C_d
80×40	0.3931	0.1978	0.1978	±1.0164	1.3415±0.0916
120×80	0.4126	0.2075	0.2075	±0.9921	1.3405±0.0958
200×150	0.4199	0.2100	0.2100	±0.9994	1.3525±0.0989
(Roshko 1954[22])		0.2075			
(Goldstein 1938[23])		0.2066			
384×96 (Alonso 1995[12])	0.46735	0.23313		1.14946(C_{lmax})	1.31523(C_{davg})

5.1.2 Oscillating Cylinder

The elastically mounted cylinder is represented by the structural model sketched in Figure 1 and the corresponding structural equations are given in section 3.1. The laminar Navier-Stokes equations are solved due to the low Reynolds number.

After a temporally periodic solution is reached, the cylinder is set to free in both streamwise and transverse directions. For the purpose of comparison with the experimental data of Griffin[24] several different combinations of structural parameters are used in the computations.

Morton et al.[13] suggested to use the reduced velocity $\bar{u} = \frac{1}{\pi St}$ such that the structural oscillator works under or near the resonance conditions. Therefore the computed St number from the stationary cylinder is used to determine $\bar{u}$. For all the cases of oscillating cylinder, St is set to be 0.2, corresponding to $\bar{u} = 1.5915$. Different mass ratios, μ_s, are used to test the different responses of the structural system. They are equal to 1.2732, 5.0, and 12.7324 respectively. To match the wide range of the experimental data, damping ratio, ζ, is chosen from the range between 0.001 - 1.583.

The dimensionless physical time step $\Delta t = 0.05$ is used, which corresponds to approximately 100 time steps per period determined by the Strouhal number used. The CFL number for the pseudo time steps varies from case to case. For the large cylinder movement cases, smaller pseudo time steps are used to limit the displacement of the cylinder during each iteration. For most of the cases the CFL number is about 500.

Figure 6 and 7 display the computed vorticity contours around the oscillating cylinder with small and large oscillation amplitude respectively. It can be seen that for the small amplitude case, the vortexes keep their coherent shedding pattern similar to the one generated by the stationary cylinder. Once the vibrating displacement becomes large, the coherent shedding of the vortexes is broken and the vortex structure becomes very irregular.

A typical time history of the drag and lift coefficients is plotted in Figure 8 with $\mu_s = 5$ and $\zeta = 0.0403$. It shows that the amplitude of the drag coefficient grows from a smaller value at the beginning and reaches a larger periodic equilibrium. In other words, the drag coefficient becomes larger as the streamwise displacement of the cylinder exists. On the contrary, the amplitude of the lift coefficient is gradually reduced from its initial value computed for the fixed cylinder. This phenomenon is called the amplitude-limiting effect[25], and can be observed in almost all the simulations for which the cylinder is in motion.

A typical trajectory of the center position of the moving cylinder is plotted in Figure 9, which is very similar to the results computed by Blackburn et al.[25] and Alonso et al.[12]

All the numerical results for present study are plotted in Figure 10 for three values of μ_s, they are equal to 1.2732, 5.0, and 12.7324 respectively. Also plotted are the computations of Alonso et al. [12] with $\mu_s = 5.0$, computations of Morton et al.[13] with $\mu_s = 12.73$, and the experimental data of Griffin[24]. In the figure, the abscissa is the reduced damping with the form of $8\pi^2 St^2 \zeta \frac{m}{\rho D^2}$[25], and the ordinate is the cross-flow displacement of motion normalized by the diameter of the cylinder. Overall, very good agreement is observed between the present results and the experimental results, especially for the case of $\mu_s = 1.2732$.

The figure shows that the higher values of mass ratios ($\mu_s = 5.0$ and $\mu_s = 12.7324$) give less satisfactory results as those with $\mu_s = 1.2732$, particularly at low damping ratios. However, they are similar to the results of Alonso et al.[12] ($\mu_s = 5.0$), and the results of Morton et al.[13] ($\mu_s = 12.73$).

The solution of the structural equations are easier to converge with a higher convergence rate compared to the fluid solution. The number of pseudo time steps taken during one physical time step varies from case to case. On the average, about 20 - 100 pseudo time steps are needed to reduce the residuals of both systems to machine zero. Figure 11 shows a typical convergence history of L_2 norm residuals of both the fluid and structural systems versus iteration number during one physical time step for the case of vortex-induced oscillating cylinder. The residual of CFD in the figure is the the maximum residual over all the grid points of the flow field.

5.2 Steady State Flow of Transonic RAE 2822 Airfoil

As the validation of the code for transonic airfoil, the steady state solution of the transonic RAE 2822 airfoil is calculated first. The freestream condition for this study are listed in Table 2 below.

Table 2: Free-stream condition for RAE 2822 Airfoil

Mach number	Static Pressure (psia)	Temperature (R)	Angle-of-Attack (deg)	Reynolds Number
0.729	15.8073	460.0	2.31	6.5×10^6

The turbulence is calculated by the Baldwin-Lomax model. This case is run using an O-type grid with three different dimensions, they are 128×50×1, 256×55×1, and 512×95×1 respectively. The outer boundary extends to 15 chords from the center of the airfoil. The experimental data provided by Cook et al.[26] are available for validation. The comparison of pressure coefficient on the airfoil is shown in Figure 12. Overall, very good agreement is obtained between the computation and experiment for each mesh dimension, especially for the two larger ones which appear to be sufficient to capture the shock on the suction surface of the airfoil without using any limiter. The important aerodynamic coefficients from both simulation and experiment are summarized in Table 3.

Table 3: Aerodynamic coefficients and $y+$ for RAE 2822 Airfoil

Mesh Dimension	C_d	C_l	C_m	$y+$
128×50	0.01475	0.73790	0.09912	0.0304 - 2.4070
256×55	0.01484	0.74036	0.09914	0.1813 - 2.3649
512×95	0.01354	0.74929	0.09861	0.0559 - 1.7569
Prananta et al.[8]	0.01500	0.74800	0.09800	
Experiment	0.01270	0.74300	0.09500	

In summary, the predicted lift coefficient agrees accurately with the experiment. The computed drag and moment coefficients also agree well with the experiment, but with larger errors.

5.3 Forced Pitching NACA 64A010 Airfoil

For this transonic airfoil, the Reynolds averaged Navier-Stokes equations with Baldwin-Lomax turbulence model are solved. Similar to the previous computation of the flow over the stationary airfoil, an O-type mesh

consisting of 280×65 cells is employed for the computations of forced pitching airfoil. The NACA 64A0101 airfoil is selected for this calculation because the experimental data is available. The fine mesh zone or the non-deforming part of the mesh is shown in Figure 13. The first grid point adjacent to the wall has the maximum $y^+ \leq 3.46$

The NACA 64A0101 airfoil is forced in pitch around its quarter chord sinusoidally. The angle of attack is imposed as a function of time as $\alpha(t) = \alpha_m + \alpha_o sin(\omega t)$, where α_m and α_o are the mean angle of attack and the amplitude of oscillation respectively. The ω is the angular frequency which is directly related to the reduced frequency $K_c = \frac{\omega c}{2U_\infty}$, where c is the airfoil chord, and U_∞ is the free-stream velocity. To compare with the experimental results given by Davis[27], the primary parameters used in the computation are listed as follows: $\alpha_m = 0$, $\alpha_o = 1.01°$, $Re = 1.256 \times 10^7$, $M_\infty = 0.8$, reduced frequency, $K_c = 0.202$.

Again, the computation begins with the steady state flow field of the stationary airfoil at 0 degree angle of attack with a dimensionless time step $\Delta t = 0.1$. The transition period takes about 3 cycles and the results becomes periodic in time after that. Figure 14 shows the lift oscillation versus the angle of attack after the flow field reaches its temporally periodic solution. The computed lift oscillation agrees quite well with the experiment[27], which have an evident improvement comparing with the recent result computed by McMullen et al. in 2002 [28].

Fig. 15 shows the computed moment coefficient compared with the experiment[27]. The computed moment coefficient does not agree as accurately with the experiment as the lift coefficient does. However the results are very similar to those predicted by Bohbot et al.[9] and McMullen et al.[28]. The large discrepancy between the computation and the experiment for the moment coefficient may be due to the inadequacy of the turbulence modeling, which may not predict the surface friction accurately.

5.4 Flutter Prediction for NACA 64A010 Airfoil

The structural model for the flow-induced vibration of a 2-D sweptback wing with a NACA 64A010 cross-section is described in section 3.2. This model was first introduced by Isogai [29] [29], and has been numerically investigated by several authors [2] [11] [8] [9]. The structural parameters used in this model are listed as the following: $a = -2.0$, $x_\alpha = 1.8$, $\frac{\omega_\alpha}{\omega_h} = 1$, $r_\alpha^2 = 3.48$, and $\mu = 60$. The elastic axis is located half a chord in the front of the airfoil nose.

The unsteady Reynolds averaged Navier-Stokes equations with the Baldwin-Lomax turbulence model are solved for the flow field in this study. The freestream conditions are: $Re = 1.256 \times 10^7$, $M_\infty = 0.75$ - 0.95 with a constant increment of 0.025.

Due to the symmetric profile of the NACA 64A010 airfoil, an initial perturbation is imposed to trigger the oscillating motion. The airfoil is forced to rotate sinusoidally about its elastic axis at the natural frequency in pitch ω_α with an angle of attack amplitude, $\alpha_o = 1°$. Usually the forced pitching mode lasts for 1 - 3 cycles. After that, the elastically mounted airfoil is set to be free in both plunging and pitching directions, and then the dynamic response is recorded.

In present study, the search of the transonic flutter boundary is conducted. The speed index, V^* defined as $\frac{U^*}{\sqrt{\mu}}$, is the parameter to classify damped, neutral and divergent responses of the airfoil. For a given $Mach$ number, the total pressure and temperature need to be adjusted to match the certain value of the Re number. In each case, several calculations are needed to determine the critical point on the flutter boundary using a bi-section method. At certain $Mach$ number, the flutter boundary is very 'thin', and more calculations are necessary to really capture the critical points. The dynamic response immediately after the transonic dip becomes very complex, and locating the flutter boundary in that region ($Mach = 0.875$ - 0.9) is very difficult and time-consuming.

In Figures (16) through (18) the time histories of plunging and pitching displacements at $M_\infty = 0.825$ are plotted for three different V^*. In these figures, from $V^* = 0.55$ to $V^* = 0.70$, the pictures correspond to the damped, neutral, and diverging responses respectively. The major task of calculating a flutter boundary is to locate where the neutrally stable or critical point is by looking at those pictures and determining where the neutral response occurs as the V^* varies. When the value of V^* is smaller than the critical value on the

flutter boundary, both plunging and pitching displacements decay corresponding to the damped response as shown in Figure (16). Once the value of V^* coincides with or closes to the critical value, the neutral response appears as shown in Figure (17). Any value of V^* beyond the critical value, a diverging response is expected as shown in Figure (18).

The V^* and the frequency ratio $\frac{\omega}{\omega_\alpha}$ for the flutter boundary are plotted versus $Mach$ number in Figures (19) and (20) respectively. Also plotted in the figures are the results from two other computations by Prananta et al. [8] and Bohbot et al. [9]. The $Mach$ number for the bottom of the transonic dip of 0.825 is consistent with their results. Overall, the present results compare well with those by others except that both values of V^* and $\frac{\omega}{\omega_\alpha}$ ratio are higher at high $Mach$ number side ($Mach$ = 0.925 and 0.95). The difference between the present results and the corresponding ones by others could be attributed to the different turbulent models and Re numbers used in the simulations. In present study, a fixed $Re = 12.56\times10^6$ is used in all the calculations. Prananta et al.[8] used $Re = 6\times10^6$ in the case of viscous flows. Bohbot et al. [9] didn't mention how large the Re used in the calculation of the flutter boundary. Prananta et al. [8] and Bohbot et al. [9] showed that the computed flutter boundaries are changed significantly in the presence of viscosity. That means that the viscosity plays an important role in determining the flutter boundary.

As an example of different vibration patterns, Figure (21) shows how the phenomenon called the Limit Cycle Oscillation (LCO) is developed. When LCO occurs, the system still stays in a stable mode with a finite oscillating amplitude even if the V^* is far beyond its critical point. In Figure (22), the presence of the second mode of the oscillation can be well observed. This case can also be considered as another kind of LCO since its V^* stays above the critical point and the oscillating amplitude keeps its temporally periodic pattern.

Figure (23) shows an interesting situation happened at $Mach$ = 0.875. Both plunging and pitching displacements of the system increase rapidly immediately after the airfoil is set to be free, but then gradually reach their steady state positions and stay there through the end of the computation. Under this flow condition, the aerodynamic forces and moments are balanced by the structure system. The angle of attack is stabilized at 2.87° and is in the range of the cruise point which is usually considered as steady state. This situation is only observed at $Mach$ = 0.875, and maybe named as 'standing'. This 'standing' phenomenon needs to be confirmed by experiment.

6 Conclusion

A fully coupled methodology is developed for calculating the flow-structure interaction problems and is used to predict transonic airfoil flutter. The scheme is derived using finite-volume flux-difference-split scheme of Roe with a 3rd order MUSCL type differencing.

The unsteady solutions march in time by using a dual-time stepping implicit unfactored Gauss-Seidel iteration, incorporating a local time stepping technique. The unsteady Navier-Stokes equations and the linear structural equations are fully coupled implicitly via successive iteration with pseudo time stepping, and approach the final solution in which both systems satisfy each other completely.

The moving mesh and mesh deformation strategy is based on two mesh zones. One is the fine mesh zone surrounding the solid body and moves with the solid object rigidly without deformation. The other is the coarse mesh zone surrounding the fine mesh zone which deforms due to the motion of the solid object and its adjacent fine mesh zone. The advantages of this mesh deformation strategy is that the orthogonality of the mesh near the wall is maintained and the fine mesh near the solid wall does not need to be regenerated to save CPU time. The computed cases have shown that such mesh deformation method has no difficulty in dealing with very large structural displacement.

For an elastically mounted cylinder, various cases with different structural parameters have been calculated. Compared with the available experimental data, the numerical results show that the important characteristics, such as cross-flow displacement, the motion of the cylinder, etc., are well predicted.

For the forced pitching NACA 64A010 airfoil, the computed lift oscillation agrees very well with the

experiment. The computed moment oscillation has large deviation from the experiment, but the results are in the similar accuracy order as other researchers have achieved. The discrepancy is considered due to the inaccurate prediction of the surface shear stress caused by the inadequacy of the turbulence modeling. The same airfoil then has been calculated as an elastically mounted airfoil with flow induced vibration. Three different responses, namely damped, neutral, and diverging response are well simulated. The flutter boundary is obtained with the transonic dip and agree well with the results of other researchers. The other phenomena captured including the limit cycle oscillation (LCO) and the steady state flow conditions.

In conclusion, the newly developed fully coupled fluid-structure interaction methodology is proved to be accurate, robust and efficient.

7 Acknowledgment

This work is supported by AFOSR Grant F49620-03-1-0253 monitored by Dr. Fariba Fahroo.

References

[1] R. B. Melville and S. A. Morton, "Fully Implicit Aeroelasticity on Oveerset Grid Systems ." AIAA Paper-98-0521, 1998.

[2] O. Bendiksen and K. Kousen, "Transonic Flutter Analysis Using the Euler Equations." AIAA Paper 87-0911, 1987.

[3] G. Guruswamy, "Unsteady Aerodynamic and Aeroelastic Calculations for Wngs Using Euler Equations," *AIAA Journal*, vol. 28, pp. 461–469, March 1990.

[4] E. Lee-Rausch and J. Batina, "Wing Flutter Computations Using an Aerodynamics Model Based on the Navier-Stokes Equations," *Journal of Aircraft*, vol. 33, pp. 1139–1147.

[5] M. Smith, "Flight Loads Prediction Methods for Aircraft: Vol I. Euler/Navier-Stokes Aeroelastic Method (ENS3DAE) Technical Development Summary: Version 4.0." WRDC-TR-89-3104, 1989.

[6] S. e. a. Vermeersch, "Towards Cost-Effective Aeroelastic Analysis on Advanced Parallel Computing Systems ." AIAA Paper 97-0646, 1997.

[7] S. Darracq, S. Champagneux, and A. Corjon, "Computation of Unsteady Turbulent Airfoil Flows with an Aeroelastic AUSM+ Implicit Solver." AIAA Paper-98-2411, 1998.

[8] B. B. Prananta, H. M. H. L., and Z. R. J., "Two-Dimensional Transonic Aeroelastic Analysis Using Thin-Layer Navier-Stokes Method," *Journal of Fluid and Structures*, vol. 12, pp. 655–676, 1998.

[9] J. Bohbot and D. Darracq, "Time Domain Analysis of Two D.O.F. Airfoil Flutter Using an Euler/Turbulent Navier-Stokes Implicit Solver." International Forum on Aeroelasticity and Structural Dynamics, Madrid, Spain, June 5-7, 2001.

[10] F. J. Blom and P. Leyland, "Analysis of Fluid-Structure Interaction by Means of Dynamic Unstructured Meshes." AD-Vol. 53-3, 4th International Symposium on Fluid-Structure Interaction, Aeroelasticity, Flow-Induced Vibrations and Noise, Volume I, ASME, 1997.

[11] J. J. Alonso and A. Jameson, "Fully-Implicit Time-Marching Aeroelastic Solutions." AIAA Paper 94-0056, 1994.

[12] J. Alonso, L. Martinelli, and A. Jameson, "Multigrid Unsteady Navier-Stokes Calculations with Aeroelastic Applications." AIAA Paper 95-0048, 1995.

[13] S. A. Morton, R. B. Melville, and M. R. Visbal, "Accuracy and Coupling Issues of Aeroelastic Navier-Stokes Solutions on Deforming Meshes." AIAA Paper-97-1085, 1997.

[14] R. B. Melville, S. A. Morton, and D. P. Rizzetta, "Implementation of a Fully-Implicit, Aeroelastic Navier-Stokes Solver." AIAA Paper-97-2039, 1997.

[15] F. Liu, J. Cai, Y. Zhu, A. Wong, and H. Tsai, "Calculation of Wing Flutter by a Coupled CFD-CSD Method." AIAA-2000-0907, 2000.

[16] Hoffmann, K. and Chiang, S., *Computational Fluid Dymamics*. Engineering Eduation System, 2000.

[17] B. Baldwin and H. Lomax, "Thin-Layer Approximation and Algebraic Model for Separated Turbulent flows." AIAA Paper 78-257, 1978.

[18] A. Jameson, "Time Dependent Calculations Using Multigrid with Application to Unsteady Flows past Airfoils and Wings." AIAA Paper 91-1596, 1991.

[19] P. Roe, "Approximate Riemann Solvers, Parameter Vectors, and Difference Schemes," *Journal of Computational Physics*, vol. 43, pp. 357–372, 1981.

[20] B. Van Leer, "Towards the Ultimate Conservative Difference Scheme, III," *Journal of Computational Physics*, vol. 23, pp. 263–75, 1977.

[21] P. Thomas and C. Lombard, "Geometric Conservation Law and Its Application to Flow Computations on Moving Grids," *AIAA Journal*, vol. 17, pp. 1030–1037.

[22] A. Roshko, "On the Development of Turbulent Wakes From Vortex Streets." NACA Rep. 1191, 1954.

[23] S. Goldstein, "Modern Developments in Fluid Dynamics." Clarendon Press, Oxford, 1938.

[24] O. Griffin, "Vortex-Induced Vibrations of Marine Structures in Uniform and Sheared Currents." NSF Workshop on Riser Dynamics, Uiversity of Michigan, 1992.

[25] H. Blackburn and G. Karniadakis, "Two and Three-Dimensional Vortex-Induced Vibration of a Circular Cylinder." ISOPE-93 Conference, Singapore, 1993.

[26] P. Cook, M. McDonald, and M. Firmin, "Aerofoil rae 2822 - pressure distributions, and boundary layer and wake measurements. experimental data base for computer program assessment," Tech. Rep. AGARD Report AR-138, AGARD, 1979.

[27] S. S. Davis, "NACA 64 A010 (NACA Ames Model) Oscillatory Pitching," Tech. Rep. AGARD Report No. 702, AGARD, August 1982.

[28] M. McMullen, A. Jameson, and J. Alonso, "Application of a Non-Linear Frequency Domain Solver to the Euler and Navier-Stokes Equations." AIAA Paper-2002-0120, 2002.

[29] K. Isogai, "Transonic Dip Mechanism of Flutter of a Sweptback Wing: Part II," *AIAA Journal*, vol. 19, pp. 1240–1242, September 1981.

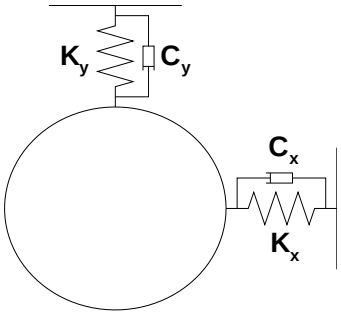

Figure 1: Sketch of the elastically mounted cy

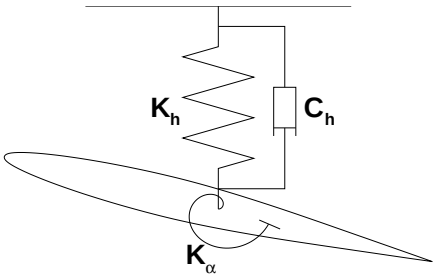

Figure 2: Sketch of the elastically mounted airfoil

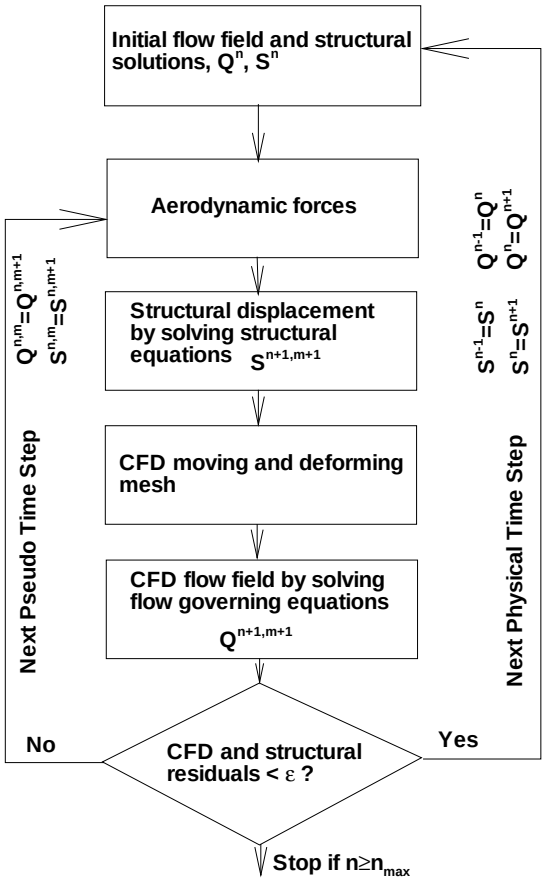

Figure 3: Flow-Structure Interaction Calculation Steps

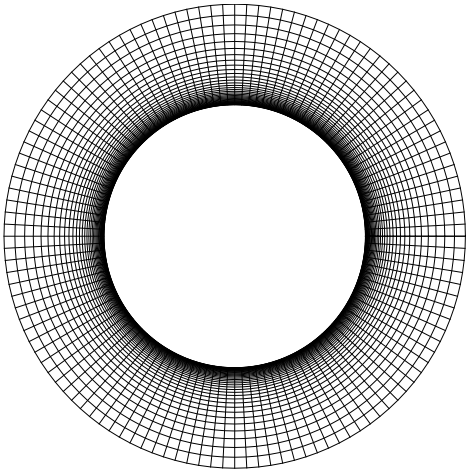

Figure 4: Mesh around the cylinder near the solid surface

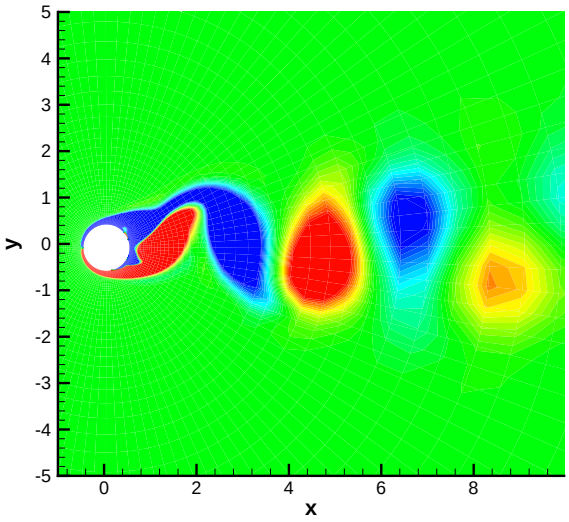

Figure 6: Vorticity contours with small cylinder structural oscillation amplitude, $\mu_s = 12.7324$, $\zeta = 0.1583$,

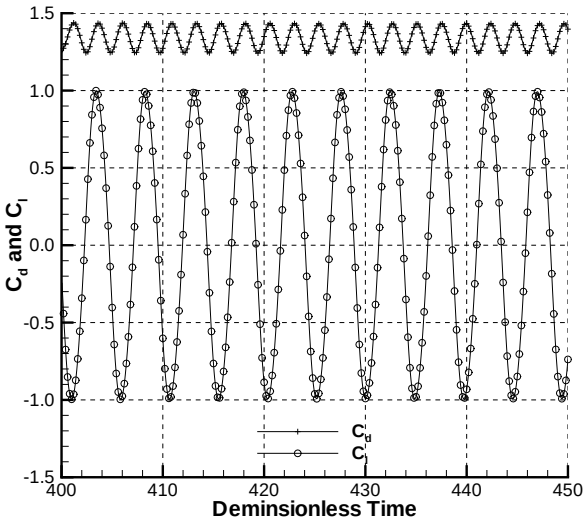

Figure 5: Time history of the lift and drag of the stationary cylinder due to vortex shedding

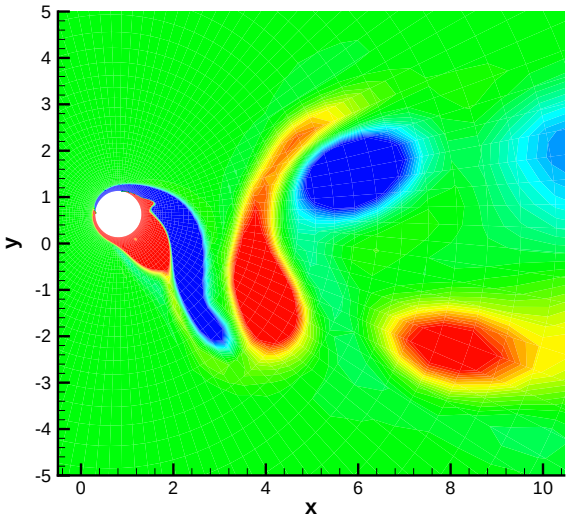

Figure 7: Vorticity contours with large cylinder structural oscillation amplitude, $\mu_s = 1.2732$, $\zeta = 0.01583$

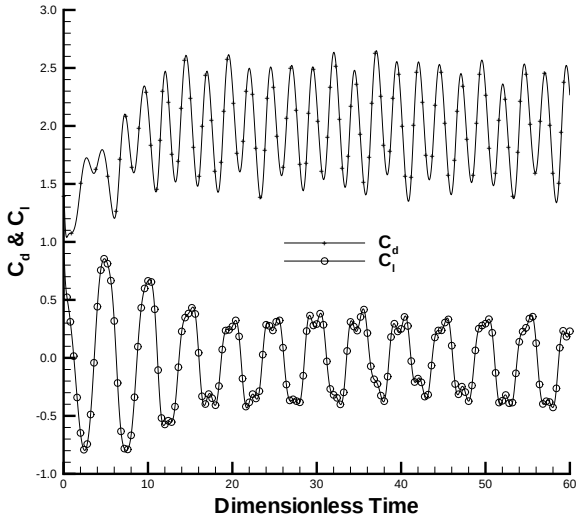

Figure 8: Time histories of the lift and drag coefficients of the oscillating cylinder, $\mu_s = 5$, $\zeta = 0.0403$

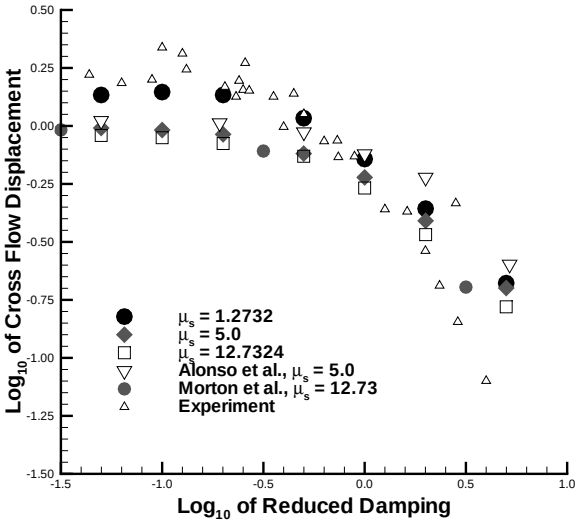

Figure 10: Comparison of the computed amplitude with Griffin's experimental data for the elastically mounted cylinder.

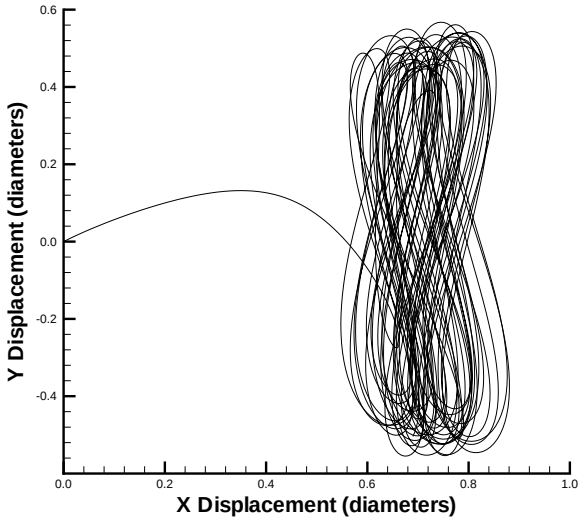

Figure 9: The trajectory of the Time histories of the lift and drag coefficients of the oscillating cylinder, $\mu_s = 1.2732$, $\zeta = 0.1583$

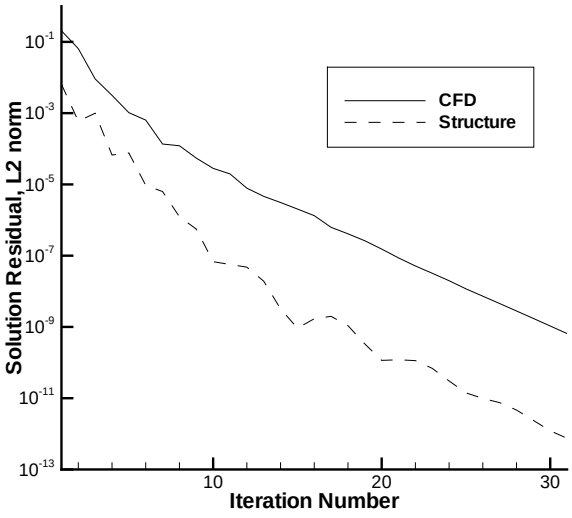

Figure 11: Convergence histories for both CFD and structural solvers within one physical time step

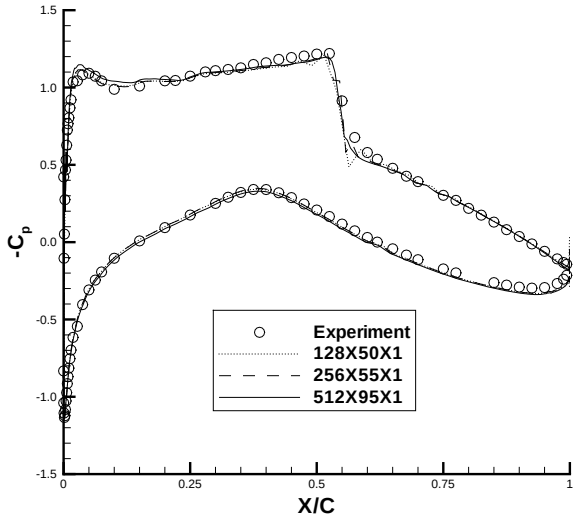

Figure 12: Pressure coefficient comparison

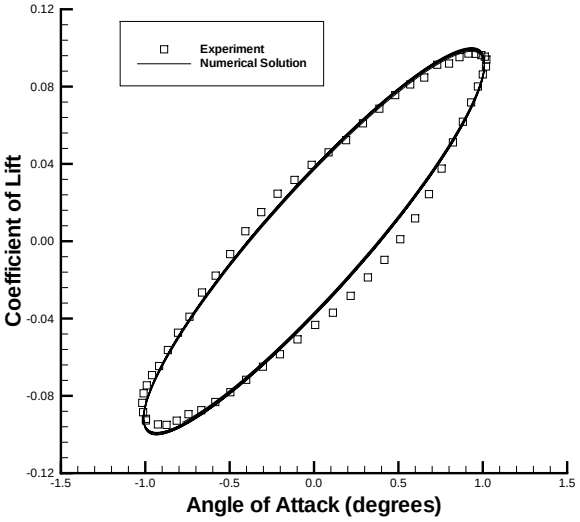

Figure 14: Comparison of computed lift coefficient with Davis' experimental data for the forced pitching airfoil.

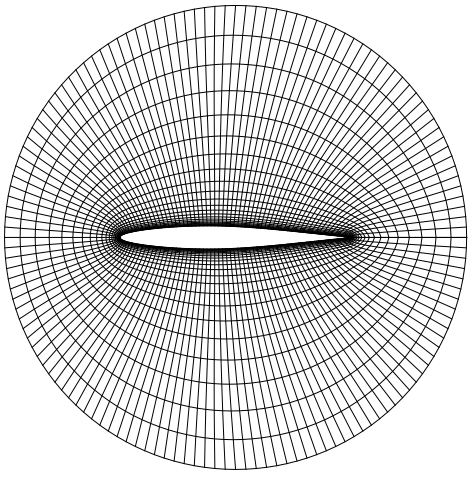

Figure 13: O-type mesh around the NACA 64A010 airfoil

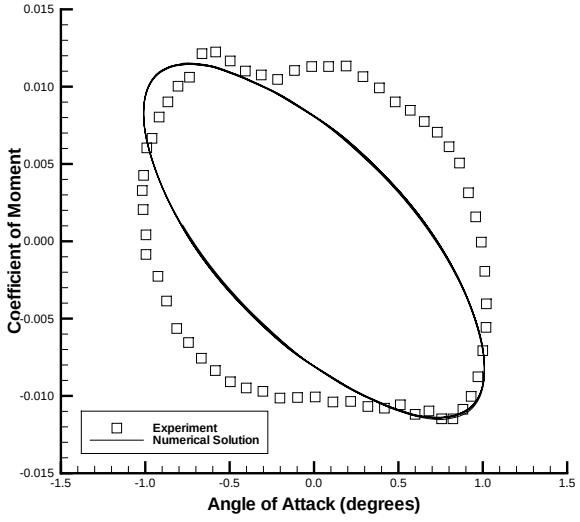

Figure 15: Comparison of computed moment coefficient with Davis' experimental data for the forced pitching airfoil.

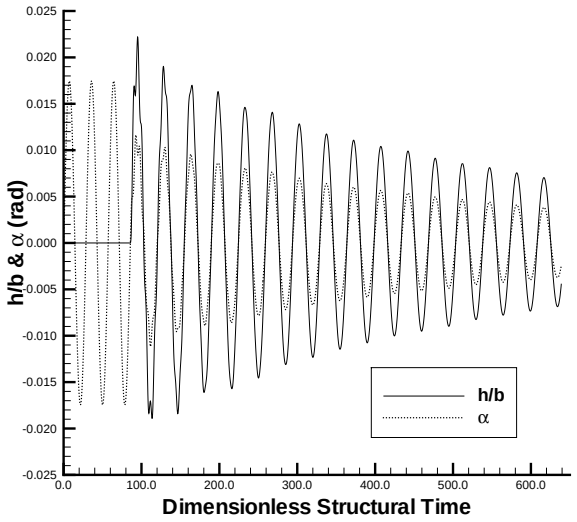

Figure 16: Time histories of plunging and pitching displacements for $M_\infty = 0.825$ and $V^* = 0.55$ - Damped response.

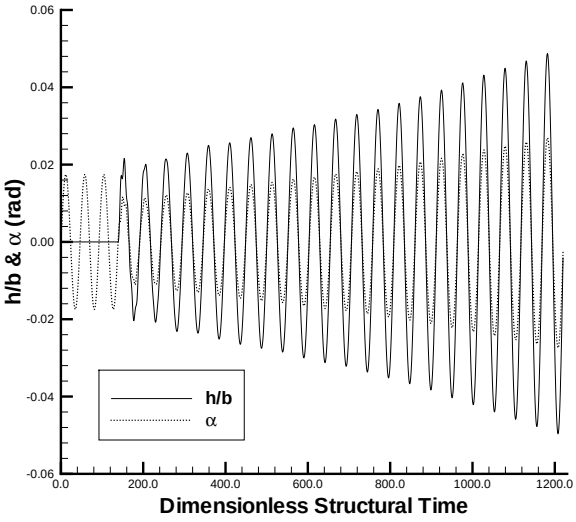

Figure 18: Time histories of plunging and pitching displacements for $M_\infty = 0.825$ and $V^* = 0.70$ - Diverging response.

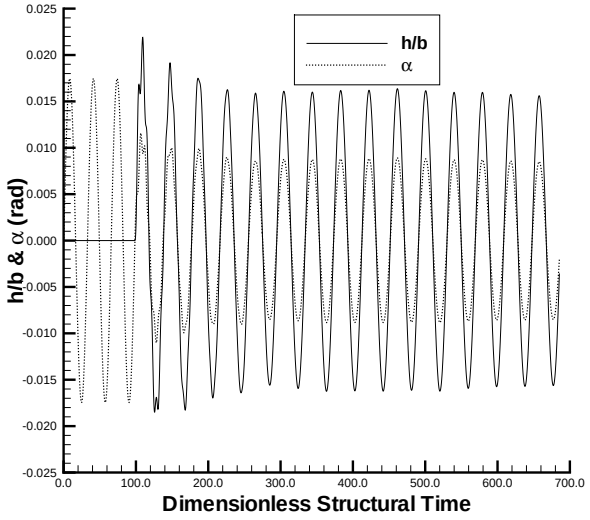

Figure 17: Time histories of plunging and pitching displacements for $M_\infty = 0.825$ and $V^* = 0.59$ - Neutrally stable response.

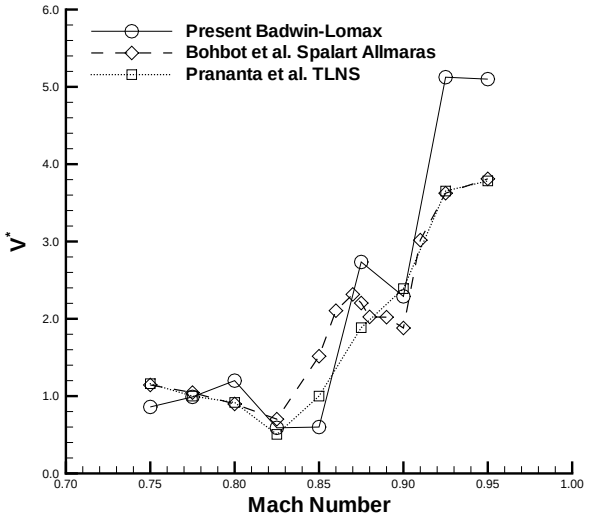

Figure 19: Comparison of computed flutter boundaries - Speed index versus Mach number.

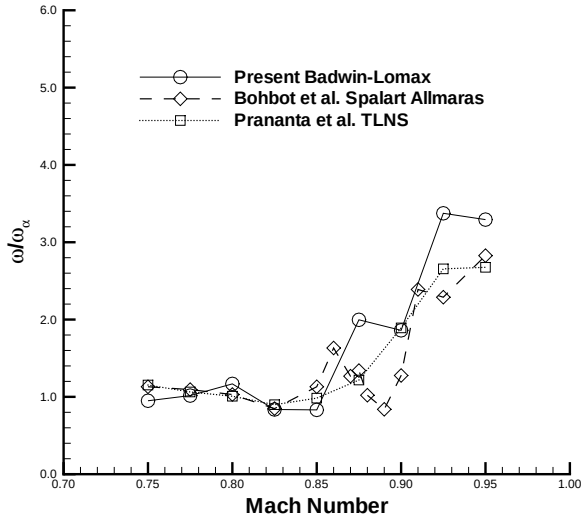

Figure 20: Comparison of computed flutter boundaries - $\frac{\omega}{\omega_\alpha}$ versus Mach number.

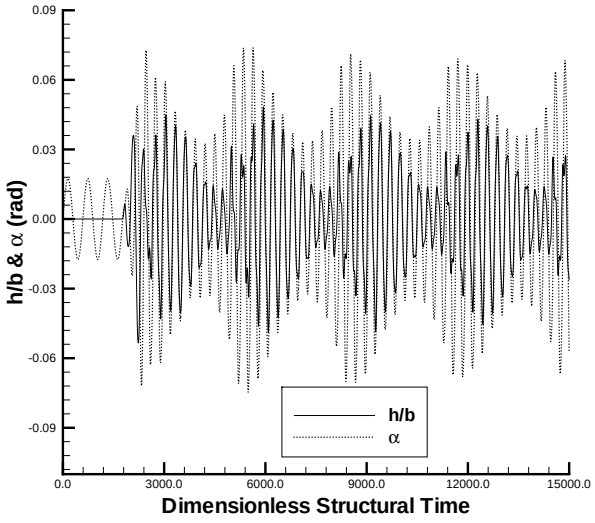

Figure 22: Time histories of plunging and pitching displacements for $M_\infty = 0.9$ and $V^* = 2.5$ - Second mode oscillation.

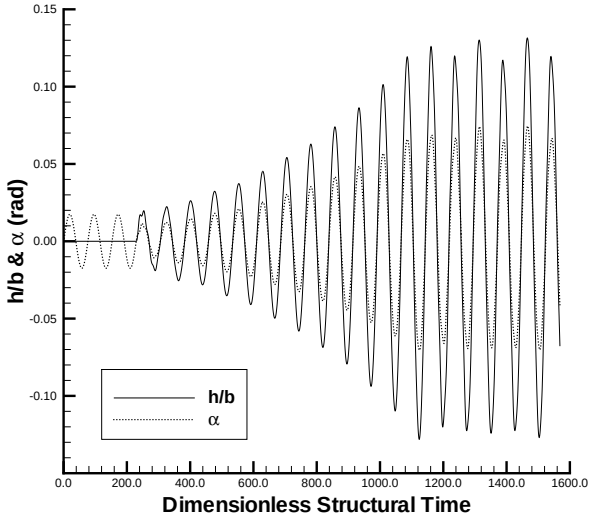

Figure 21: Time histories of plunging and pitching displacements for $M_\infty = 0.825$ and $V^* = 0.9$ - Limit Cycle Oscillation.

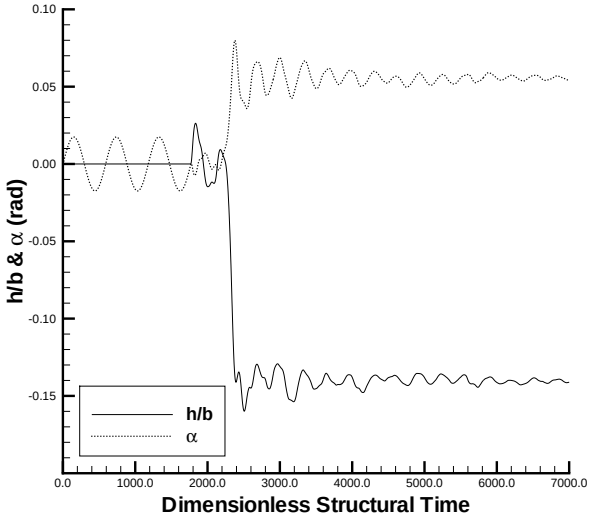

Figure 23: Time histories of plunging and pitching displacements for $M_\infty = 0.875$ and $V^* = 2.5$ - 'Standing' status.